Geochimica et Cosmochimica Acta 346 (2023) 223–230

Contents lists available at ScienceDirect

Geochimica et Cosmochimica Acta

journal homepage: www.elsevier.com/locate/gca

Nanoscale distribution of Ge in Cu-rich sphalerite

Denis Fougerouse [a,b,*], Alexandre Cugerone [c], Steven M. Reddy [a,b], Kai Luo [d], Vincent Motto-Ros [e]

[a] School of Earth and Planetary Sciences, Curtin University, Perth, Australia
[b] Geoscience Atom Probe Facility, John de Laeter Centre, Curtin University, Perth, Australia
[c] Department of Earth Sciences, University of Geneva, Geneva, Switzerland
[d] School of Earth Sciences, Yunnan University, and Key Laboratory of Critical Minerals Metallogeny in Universities of Yunnan Province, Kunming, China
[e] Institut Lumière Matière UMR 5306, Université Lyon 1 – CNRS, Université de Lyon, Villeurbanne, France

ARTICLE INFO

Article history:
Received 26 November 2022
Accepted 14 February 2023
Available online 20 February 2023
Associate editor: Georges Calas

Keywords:
Critical minerals
By-products
Exsolution
Solid-solution

ABSTRACT

A large proportion of the critical elements resources Ge, Ga, and In are associated with sphalerite in Pb-Zn ore deposits. Germanium in sphalerite has been proposed to be structurally bound in the crystal lattice. Using a combination of microstructural, geochemical and nanoscale observations, we show that Ge can be hosted in sphalerite crystal structure as well as nanoparticles of briartite ($Cu_2(Zn,Fe)GeS_4$). The structurally-bound Ge was preserved in undeformed sphalerite grains from the Saint-Salvy Pb-Zn vein deposit (France), whereas the briartite nanoparticles were observed in metamorphosed sphalerite from Arre. The briartite nanoparticles likely exsolved from sphalerite during the Pyrenean-Alpine metamorphism and deformation. The presence of nanoparticles may harden the sphalerite during crystal-plastic deformation and help to preserve the critical elements resources of Pb-Zn deposits during metamorphism.

1. Introduction

Germanium (Ge) is a metal listed as a critical mineral with high supply risk and key applications in the high-tech industry. Germanium is mainly used in fibre optics for network communication and infrared night vision applications. Sphalerite (ZnS) is the main ore mineral for the production of Zn worldwide and critical commodities such as Ge, Ga and In can be extracted from sphalerite as by-products, with the potential to improve the value-chain. In Pb-Zn deposits, Ge endowment is rarely reported using mineral resource reporting codes (e.g. JORC), and a complete understanding of its distribution in the crust in relation to the geological context is lacking. In addition, sphalerite mineralization can be hosted in metamorphosed settings, but the impact of metamorphism on by-product critical elements is rarely explored despite evidence of critical elements mobility (Cugerone et al., 2020; Tiu et al., 2021). Key to further our understanding of critical commodities and their economic potential, the spatial distribution of critical elements in Zn ores is essential.

The critical trace metals Ge, Ga and In are thought to be hosted in the sphalerite crystal lattice and several substitution mechanisms have been debated based on correlation trends from microscale analyses (Cook et al., 2009; Johan, 1988). However, there is a discrepancy between the scale of observation by classic microscale characterization techniques and the nanoscale processes controlling the incorporation and redistribution of trace elements in sphalerite. The primary and secondary mechanisms controlling the distribution of trace elements in sphalerite underpin our understanding of processes responsible for critical metals enrichment (Cook et al., 2009) and the use of sphalerite as a geothermometer (Frenzel et al., 2016). Atom probe tomography (APT) is a technique ideally suited to study the nanoscale trace element distribution in minerals (Reddy et al., 2020). APT in ore minerals have revealed the nanoscale distribution of Au in pyrite and arsenopyrite (Fougerouse et al., 2016a, 2021; Gopon et al., 2019; Wu et al., 2019a), the composition of nanoscale fluid inclusions in pyrite (Dubosq et al., 2021; Taylor et al., 2022) and the distribution of Cu, Sb and Ag in sphalerite wih rhythmic bands/sector zones (Schirmer et al., 2020). In this study, the grain- to nanometre scale distribution of trace elements in sphalerite is investigated in one undeformed sample from Saint-Salvy (Montagne Noire, France) and one partially deformed sample from Arre (Pyrenees, France)

* Corresponding author at: School of Earth and Planetary Sciences, Curtin University, Perth, Australia.
E-mail address: denis.fougerouse@curtin.edu.au (D. Fougerouse).

https://doi.org/10.1016/j.gca.2023.02.011
0016-7037/

in order to decipher the trace element incorporation and redistribution mechanisms in Cu-rich sphalerite.

2. Geological Context of Saint Salvy and Arre

Saint-Salvy and Arre deposits are hosted in the Paleozoic basement of the Montagne Noire and Pyrenean Axial Zone (PAZ), respectively, and are mostly composed of Paleozoic metasedimentary rocks, Ordovician gneiss and Carboniferous granites (Fig. 1). The region was metamorphosed during the Variscan orogeny (Carboniferous-Early-Permian; Zwart, 1963). Following the Variscan orogeny, a long period of Mesozoic crustal extension occurred mostly in the North Pyrenean Massifs (Fig. 1B) until the Early-Cretaceous (Clerc et al., 2015). During the Late Cretaceous-Miocene, a second inversion period, named the Pyrenean-Alpine orogeny, is considered to have induced limited deformation in the Variscan basement and is only recognized close to regional Pyrenean-Alpine thrusts and faults, or in post-Variscan sphalerite ore bodies.

The Mesozoic Pb-Zn epigenetic veins are widespread in the Montagne Noire (Saint-Salvy, Peyrebrune) and in the PAZ (Arre-Anglas, Cierco, Aulus-Les Argentières; Johnson et al., 1996; Munoz et al., 2016). In the western part of the Montagne Noire, the Saint-Salvy deposit is hosted in Cambrian black-shale (Munoz et al., 1994) and the mineralisation is composed of cockade breccia filled with sphalerite in a gangue of siderite and quartz (Munoz et al., 1994). These veins are likely associated with the Lias-Dogger transition during an extensive strike-slip regime (Munoz et al., 1994) and are emplaced by fluids at low-temperature (~100–150 °C) with high salinity (>15 wt% NaCl. eq.). No major tectonic event has impacted these veins and sphalerite exhibits well-formed euhedral crystals, with common primary chemical zoning (i.e., sector zoning and rhythmic bands; Belissont et al., 2014; Johan, 1988).

The Arre district is located in the western part of the PAZ, close to a Pyrenean-Alpine regional thrust (i.e. Eaux-Chaudes; Cugerone et al., 2018; Reyx, 1973). The epigenetic vein-type mineralization is frequently hosted in folded Devonian schist and limestone-marble and/or Carboniferous magmatic rocks and are parallel to the sub-vertical Variscan S2 cleavage (Fanlo et al., 1998; Reyx, 1973; Subías et al., 1999). This vein system is associated with circulation of low-temperature (<150 °C) and high-salinity (>15 wt% NaCl. eq.) hydrothermal fluids during the Mesozoic (Cugerone et al., 2021). These veins have endured plastic deformation and partial recrystalisation at low grade (<400 °C) after the Variscan orogeny (post D2-M2 metamorphism), probably during the Pyrenean-Alpine deformation (Cugerone et al., 2020, 2021). The Ge mineral Briartite ($Cu_2(Zn,Fe)GeS_4$) has been reported at sphalerite grain boundaries in recrystallized domains or along twin boundaries in sphalerite parent grains at Arre, whereas other Ge minerals such as brunogeierite ($GeFe_2O_4$), carboirite ($GeFeAl_2O_5(OH)_2$), or argutite (GeO_2) have been observed in older, late-Variscan veins (Cugerone et al., 2021).

3. Methods

3.1. Electron Backscatter Diffraction (EBSD)

In sulphides, the distribution of trace elements can be affected by deformation microstructures and its quantification is therefore important (Fougerouse et al., 2019, 2021; Reddy and Hough, 2013). The quantification the distortion of sphalerite crystals was conducted using EBSD. Amongst other information, EBSD can determine the amount of crystal-plastic deformation, the distribution of low-angle, twin and grain boundaries. EBSD analyses were performed with a Camscan Crystal Probe X500FE scanning electron microscope (SEM) equipped with an Oxford Instruments Symmetry EBSD detector at the University of Montpellier/CNRS. One sample from each case study was investigated with EBSD. The data was processed using the Oxford Crystal software.

3.2. Laser-Induced Breakdown Spectroscopy (LIBS)

Laser-Induced Breakdown Spectroscopy (LIBS) multi-elemental imaging was performed at the Institute Lumière Matière, University of Lyon 1 (France; Cáceres et al., 2017). The two samples were analysed using a nanosecond Nd:YAG laser with a pulse energy of 600 μJ operating at 100 Hz at the fundamental wavelength (1064 nm). A 15× magnification lens (LMM-15X-P01, Thorlabs, Germany) was used to focus the laser pulses on the sample surface. In this configuration, the size of the ablation craters for a single laser shot was in the range of 8 μm. In the shown images, the lateral resolution (step size) was 19 μm. All experiments were conducted at room temperature under ambient pressure conditions. In addition, the laser pulse energy and its focus onto the sample were strictly controlled.

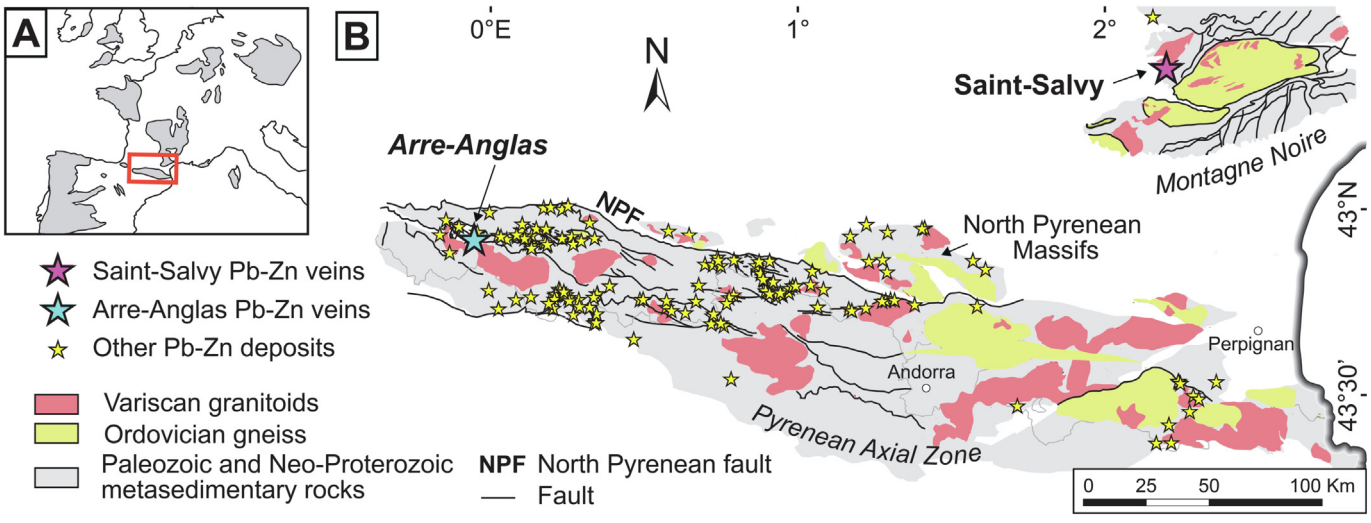

Fig. 1. (A) Simplified geological map of western Europe; (B) Geological map of the Pyrenean Axial Zone (PAZ) and Montagne Noire (modified after Cugerone et al., 2020).

Two spectrometers were configured to detect intense lines of Ge, Cu, Ga, Ag, Fe, Sn and In, all localised in the spectral range from 260 to 330 nm. The line wavelengths used for these different elements are reported in supplementary Table 1. The general protocol used for the construction of the elemental images has been described in Motto-Ros et al. (2019). Briefly, the line intensities (associated with the elements of interest) were retrieved for each sample position (i.e., spectrum) by defining a baseline on a spectral range of a few nanometers and subtracting it from the emission line of interest. One sample from each case study was investigated with LIBS.

3.3. Atom probe tomography (APT)

APT analyses were conducted at the Geoscience Atom Probe facility, John de Laeter Centre, Curtin University (Reddy et al., 2020). Six specimens from Arre and three from Saint-Salvy were analysed by APT. The instrument, a Cameca LEAP 4000X HR, was operated in laser assisted mode with a UV (λ = 355 nm) laser, a laser pulse energy of 30 pJ and a repetition rate of 200 kHz. The base temperature was maintained at 30 K and the automated detection rate at 0.02 ion/pulse.

The APT mass spectra is relatively complex with the presence of overlapping peaks such as Zn^{2+} and S^{+} rendering the major element quantification challenging (Fig. S1). Other isobaric interferences include $^{70}Zn^{+}$ and $^{70}Ge^{+}$ for example. In this study, the quantification of major elements was not investigated. For the quantification of trace elements, Ag was measured as both $^{107}Ag^{+}$ and $^{109}Ag^{+}$, Sb as $^{121}Sb^{+}$ and $^{123}Sb^{+}$, Ga as $^{69}Ga^{+}$ and $^{71}Ga^{+}$, In as $^{113}In^{+}$ and $^{115}In^{+}$ and Sn as Sn^{++}. Because of isobaric overlaps between $^{70}Zn^{+}$ and $^{70}Ge^{+}$, $^{70}Zn^{32}S^{+}$ and $^{70}Ge^{32}S^{+}$ or, $^{70}Zn^{32}S_2^{+}$ and $^{70}Ge^{32}S_2^{+}$, Ge was quantified using the abundance of ^{74}Ge peaks and normalised to the natural isotopic abundance of Ge. The background of the ^{65}Cu peaks is systematically elevated and variable due to the thermal tails of the ^{64}Zn peaks. Therefore, Cu was normalised to natural isotopic abundance from measuring the ^{63}Cu peaks at Cu^{++}, Cu^{+}, CuS^{+} and CuS_2^{++}.

The data was reconstructed in 3 dimensions using Cameca's AP Suite 6 software. For the voltage-based reconstruction of sphalerite, the atomic volume was calculated at 0.01976 nm^3/atom and a field evaporation value was determined empirically at 16.9 6 ± 0.04 V/nm (Fougerouse et al., 2022). The quantification of trace elements from APT data is further detailed in supplementary materials.

In order to investigate for spatial heterogeneities, a near neighbour analysis was performed and compared to a simulated random distribution of atoms (Fig. S2; Philippe et al., 2009). For the near neighbour analysis, the order was set to 1, the d_{pair} to 3.5 nm for Cu and 6 nm for Ag, and the d_{pair} sample width to 0.05 nm for Cu and 0.15 nm for Ag. We further use the χ^2 and Pearson coefficient (μ) statistical tests to quantify the variation from randomness as described elsewhere (Perea et al., 2015; Taylor et al., 2022).

Although APT has a limited lateral field of view (~100 nm), correlative techniques such as EBSD and LIBS provide the mineralogical and geochemical context of the APT specimen. In turns, this provides confidence that the nanoscale observations are representative of the textural domains analysed. More discussion on this subject can be found in Reddy et al. (2020).

4. Results

In the Saint-Salvy sample, the sphalerite crystals are subhedral and preserve primary growth zoning features such as rhythmic bands and sector zoning as marked by colour variations in the transmitted light microscopy image (Fig. 2A). The EBSD data indicate the presence of {111} growth twins crosscutting through weakly deformed crystals. Local low-angle misorientations (<5°) appear close to grain boundaries or twins (Fig. 2B). The LIBS image reveals that the darker regions, i.e. sector zones, observed in the transmitted light micrograph are enriched in Cu and Ge (Fig. 2C&D) as well as Ag, Ga and Sb (Fig. S3). A sector zone enriched in trace elements was selected for APT analyses (Fig. 2).

The APT 3D atom maps of the Saint-Salvy sample reveal subparallel bands at the 5 to 10 nm scale alternatively enriched in trace elements such as Ga, Cu, Ge, Sb and Ag (Fig. 3). Along bands rich in trace elements, the Ag distribution is further heterogeneous with small (<2 nm) clusters enriched in Ag and Cu (Fig. 3A inset). The clustering of Ag and Cu is further demonstrated by a near neighbour analysis (Fig. S2). For Ag, an experimental χ^2 = 15753 is determined, far greater than the theoretical χ^2 of 55.7 with 40

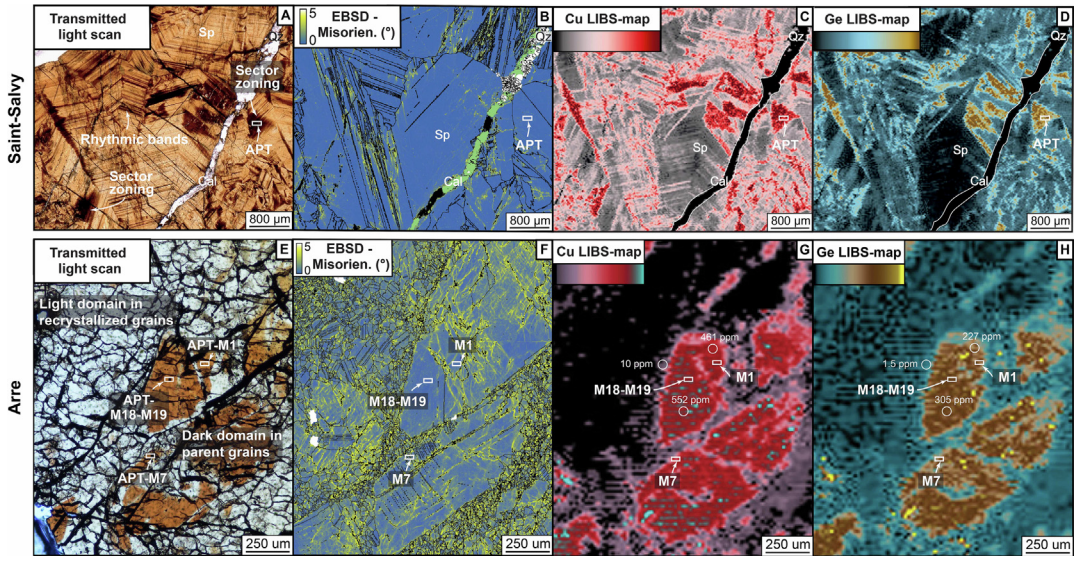

Fig. 2. Sphalerite texture and distribution of Cu and Ge in sphalerite from the Saint-Salvy and Arre deposits. Using transmitted light scan (A) and EBSD map (B), sphalerite texture is poorly deformed in Saint-Salvy and highly deformed in Arre (E&F). In the same area, LIBS maps (quantified with LA-ICP-MS analyses for Arre only) show very heterogeneous Cu and Ge distribution, with sector zoning enriched in Cu (C) and Ge (D) at Saint-Salvy and Cu-Ge rich dark domains at Arre (G&H) with local occurrence of Cu-Ge minerals. Light domains are generally poorly enriched in Cu and Ge in the two types of sphalerite. The location of the APT specimens are indicated.

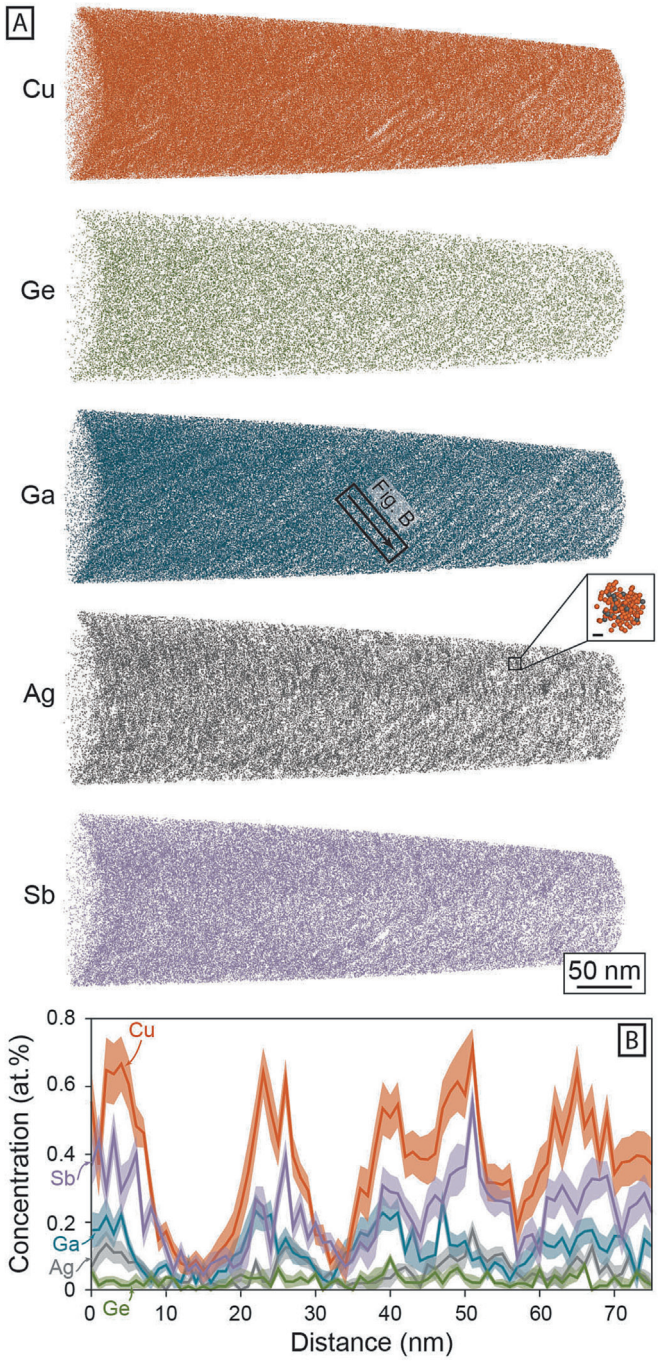

Fig. 3. (A) Atom probe tomography (APT) 3D atom maps of the Saint-Salvy specimen M22. Each sphere represents one ion. The sphalerite displays fine banding in trace elements of all elements. Inset: Ag (grey) is hetereogeneous along banding with small clusters also enriched in Cu (orange). The scale bar is 2 nm; (B) 1D concentration profile showing the fine trace element banding. (For interpretation of the references to colour in this figure legend, the reader is referred to the web version of this article.)

degrees of freedom and 95% confidence level. For Cu, the experimental χ^2 is 9522 and is greater than the theoretical χ^2 of 90.5 with 70 degrees of freedom and 95% confidence. For both elements, the Pearson coefficient μ equals to 1, indicating a strong deviation for randomness and clustering. The Ge concentration of the Saint-Salvy whole APT specimens varies from 255 to 481 ppma. The combined Cu and Ag concentration ranges between 6379 and 6901 ppma whereas the combined Sb, Ga, In, Ge and Sn concentration ranges 3475 to 3629 ppma (Fig. 5 and Table 1).

In the Arre sample, the sphalerite crystals are anhedral and only dark and light-brown patchy domains can be observed with no clear growth textures (Fig. 2E). The EBSD data indicates the presence of numerous small grains (<50 μm) in recrystallised domains, surrounding larger grains (>250 μm) with low amount of misorientation (<15°; Fig. 2F). In transmitted light, the recrystallised grains appear light in colour whereas the large weakly deformed grains appear dark (Fig. 2). The LIBS maps indicate that the dark domains in large grains are enriched in Cu and Ge, whereas the recrystallised light-brown domains are poor in trace elements (Fig. 2G&H). High intensity signal on the LIBS maps are indicative of Ge minerals, mainly along fractures. Three different areas in Ge-Cu-rich domains characterised by a relatively low amount of disorientation were selected for APT (Fig. 2).

The whole specimen APT data of the Arre sample reveals that the trace element composition is dominated by Cu and Ge with below detection limit amounts of Ga, Sb, In and Sn (Table 1). The APT data are heterogeneous with variable sized spherical domains from 10 nm to 75 nm in diameter in all grains analysed (Fig. 4). In average, the spherical domains are enriched in Cu (~21.6 at.%), Ge (~9.0 at.%), and Fe (~12.4 at.%), and depleted in Zn (~4.3 at.%; Fig. 5 and Table 1). The concentration of Ge in the matrix surrounding the Ge-rich spherical particles could not be determined above background noise. The composition of whole APT specimens (spherical domains and matrix combined) range between 509 and 2653 ppma Cu, and 233 to 1104 ppma Ge (Fig. 5 and Table 1). No Cl was detected above the background in the Arre and Saint-Salvy samples.

5. Discusion

5.1. Bimodal distribution of Ge in sphalerite

The APT data of the Saint-Salvy sample indicate that trace elements, including Cu, Ge, Ga and Sb are distributed homogeneously along fine oscillatory growth bands (Fig. 3). The fine trace element oscillatory zoning is similar to As-Au-Cu zoning observed in arsenian pyrite and interpreted to reflect the diffusion-limited self-organization of ions at the crystal-fluid interface (Putnis et al., 1992; Wu et al., 2019a). Such trace element distribution implies that these metals are hosted within the crystal structure of sphalerite, or solid solution, as previously suggested. The speciation of Ge in sphalerite has been determined to be either tetravalent or bivalent (Belissont et al., 2016; Bonnet et al., 2017). In the Cu-rich systems of Saint-Salvy, Ge (IV) is prevalent and the substitution type (1) has been suggested (Belissont, 2016; Belissont et al., 2016; Wei et al., 2019; White et al., 2022).

$$3Zn^{2+} \leftrightarrow Ge^{4+} + 2(Cu, Ag)^{+} \quad (1)$$

However, additional trace elements such as Ga, In, Sb, Sn, As, Tl and Cl are likely contributing to the charge balance (Belissont, 2016; Cook et al., 2009; Frenzel et al., 2020; Johan, 1988; Schirmer et al., 2020). The APT data is consistent with substitution mechanism (1), however an excess of Ag and/or Cu is notable from the APT data (Fig. 5) and was also noted by (Belissont et al., 2014). The APT results reveal the presence of Ag-Cu clusters with no Ge, only a few nanometre in diameter (Fig. 3A inset). The composition of these clusters is difficult to determine due to their small size and potential analytical artefacts such as ion trajectory aberrations (Reddy et al., 2020). The presence of these precipitates would contribute to the Ag-Cu excess, but mass balance calculations cannot yet quantify their influence. The formation mechanism of the pre-

Table 1
APT trace element composition of sphalerite and major element composition of briartite nanoscale inclusions.

Whole APT specimens trace element composition (in ppma):

	Cu	1σ	Ag	1σ	Sb	1σ	Ga	1σ	Ge	1σ	Sn	1σ	In	1σ	Fe	1σ
St Salvy M20	6491	267	410	88	1626	177	729	137	255	53	819	134	–	–	22768	695
St Salvy M21	5940	298	439	105	1957	223	1048	180	457	72	147	95	–	–	26038	847
St Salvy M22	6031	261	507	98	2245	204	741	145	481	65	108	79	–	–	25906	756
Arre M1	509	213	–	–	–	–	–	–	233	128	–	–	–	–	32621	1801
Arre M3	1437	162	–	–	–	–	–	–	514	72	–	–	–	–	32713	829
Arre M7	1687	306	–	–	–	–	–	–	635	127	–	–	–	–	31702	1436
Arre M10	690	181	–	–	–	–	–	–	211	82	–	–	–	–	31283	1314
Arre M18	1378	271	–	–	–	–	–	–	484	114	–	–	–	–	31760	1424
Arre M19	2653	319	–	–	–	–	–	–	1104	137	–	–	–	–	32412	1221

Briartite inclusions composition (in at.%):

	Fe	1σ	S	1σ	Cu	1σ	Zn	1σ	Ge	1σ
Arre M1-1	11.4	0.7	55.9	1.1	18.6	0.9	5.7	0.5	8.1	0.6
Arre M1-2	11.2	2.5	55.7	4.0	17.8	3.1	6.7	2.4	8.3	2.2
Arre M1-3	9.8	0.9	59.2	1.5	17.4	1.2	6.4	0.8	7.1	0.8
Arre M3-1	12.6	0.2	50.5	0.3	24.2	0.3	3.6	0.1	8.9	0.2
Arre M3-2	13.1	0.7	50.0	1.1	23.9	1.0	2.8	0.5	10.0	0.6
Arre M3-3	11.1	1.3	54.9	2.0	19.6	1.7	6.2	1.0	8.0	1.1
Arre M7-1	14.3	0.3	47.9	0.4	25.1	0.3	2.1	0.1	10.4	0.2
Arre M7-2	12.6	0.7	52.3	1.1	20.9	0.9	5.0	0.5	8.9	0.6
Arre M19-1	13.9	0.2	48.5	0.3	24.6	0.3	1.4	0.1	11.4	0.2
Arre M19-2	14.1	1.4	49.5	2.0	23.9	1.7	3.2	0.8	9.0	1.1
Average	12.4		52.4		21.6		4.3		9.0	

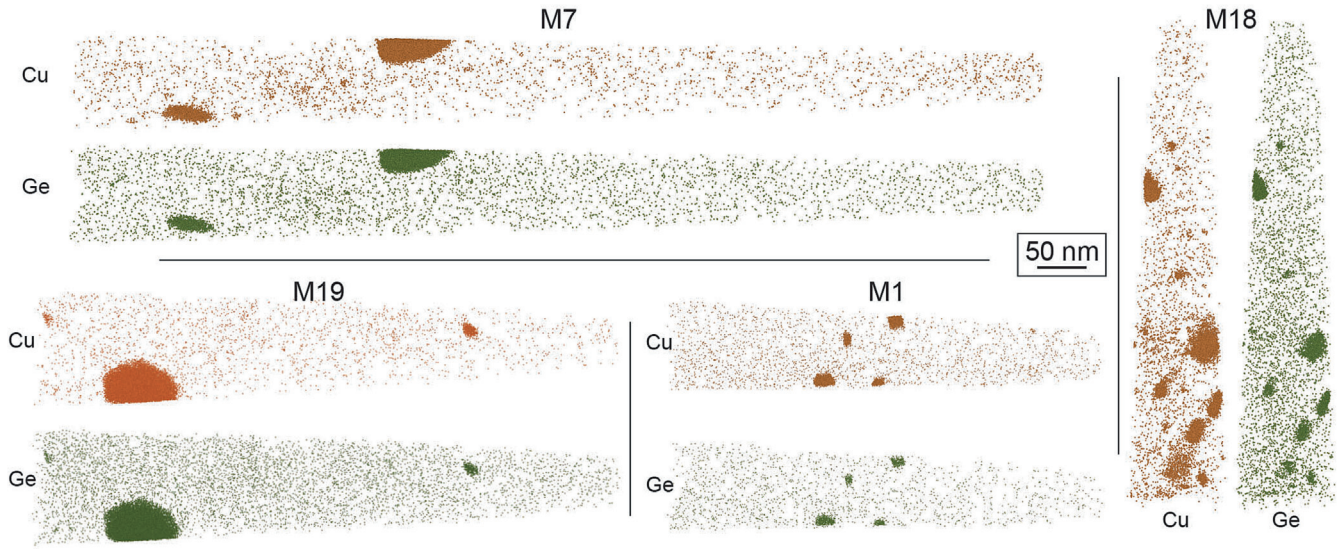

Fig. 4. Atom probe tomography (APT) 3D atom maps of the Arre specimens M1, M7, M18 and M19. Each sphere represents one ion. The Arre Cu and Ge distribution is heterogenous with nanoscale clusters of briartite ($Cu_2(Zn,Fe)GeS_4$).

cipitates is currently unclear. They could have formed during sphalerite crystallisation or during local reequilibration following rapid crystallisation.

In the Arre sample, the APT data reveals the presence of Cu-Ge-rich 10 nm to 75 nm diameter clusters. These clusters have a composition consistent with nanoscale inclusions of briartite ($Cu_2(Zn,Fe)GeS_4$). Excluding the Cu-Ge clusters, in the sphalerite matrix, the concentration of Ge is below the detection limit of APT in the three sphalerite domains analysed. Therefore our results suggest that the majority, if not all, of the Ge in the Arre sphalerite is hosted in briartite nanoscale inclusions (Fig. 6). Briartite grains greater than 5 μm in diameter have been observed in Arre samples along sphalerite grain boundaries in recrystallized domains (Cugerone et al., 2020), but nanoscale briartite inclusions have not been reported before in sphalerite. In a previous study on the geochemistry of the Arre sphalerite, a substitution mechanism $2Zn^{2+} \leftrightarrow 2Cu^{+} + Ge^{4+}$ was proposed based on a 2Cu = Ge relationship in correlation plots from LA-ICP-MS data (Cugerone et al., 2021). In these data, the time-resolved output graphs were free of spikes (Cugerone et al., 2021) and the Ge signal could not be attributed to the presence of discrete mineral inclusions (Gregory et al., 2015). Instead, the nanoscale observations by APT from the same sphalerite grain indicate that the 2Cu = Ge relationship in the Arre sample is due to briartite nanoscale inclusions. In briartite, Ge is also tetravalent, in agreement with previous studies (Belissont et al., 2016). However, our results do not explain the observation of Ge (II) in sphalerite from Tennessee and the Tar Creek Superfund Site, Oklahoma (Bonnet et al., 2017; White et al., 2022), suggesting that Ge may be hosted through separate substitution mechanisms or by nanoscale heterogeneities not documented in this study. A study of samples from different deposit types formed by different processes may reveal additional miner-

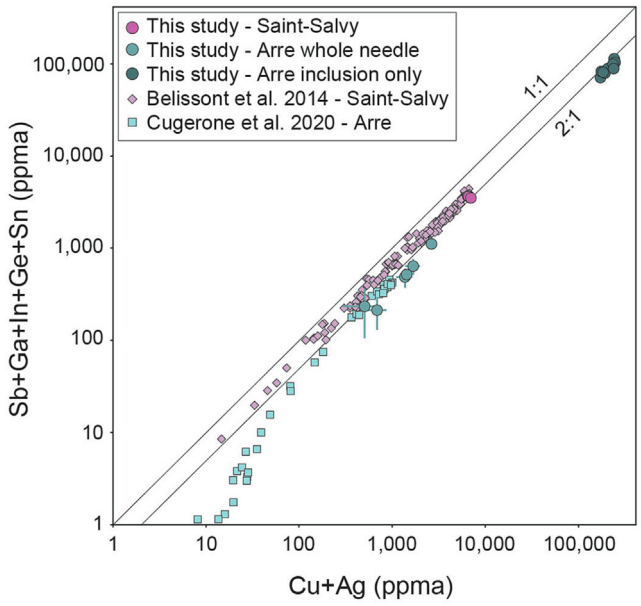

Fig. 5. Sb + Ga + In + Ge + Sn vs Cu + Ag content. The data of Bélissont et al. (2016) and Cugerone et al. (2021) were acquired by LA-ICPMS whereas the data from this study are from APT measurements.

alogical locations for Ge in sphalerite, including sphalerite with a strong correlation between Fe and Ge (Baele et al., 2021; Cook et al., 2009; Luo et al., 2022).

5.2. Nanoscale remobilization of Ge

The nanoscale briartite inclusions in the Arre sphalerite may be the result of local Ge and Cu redistribution during recrystallization (Cugerone et al., 2020) or may form through a primary precipitation process during recrystallization. In this last hypothesis, the precipitation of a high density of small briartite crystals from the mineralising fluid would imply a high nucleation rate and Ge supersaturation with concomitant precipitation of sphalerite and encapsulation of the briartite nanoscale crystals. However, the absence of large briartite grains in equilibrium with sphalerite and the significant Ge concentration of sphalerite suggests that briartite precipitation through a primary precipitation process is unlikely.

The Arre deposit was affected by metamorphism during the Pyrenean-Alpine orogeny (Cugerone et al., 2021), and several mechanisms have been proposed to explain the remobilisation of trace elements in minerals during metamorphism, including fluid-mediated dissolution-reprecipitation (Putnis, 2002), and diffusion processes such as solid-state (volume) diffusion, short-circuit diffusion, and defect-impurity pair diffusion (Mehrer, 2007).

The fluid-mediated dissolution-reprecipitation process can change the overall chemistry of sulphides (Fougerouse et al., 2016b; Wu et al., 2019b; Xia et al., 2009). In the Arre sphalerite, the interplay between diffusion and dissolution-reprecipitation has been interpreted to be responsible for Ge remobilisation (Cugerone et al., 2021). Textural characteristics of dissolution-reprecipitation include curviplanar or finger-like reaction fronts, porous replaced domains, and the loss of impurities in the reacted phase (Putnis, 2002). However, these characteristics are not present in the large, weakly deformed and trace element rich sphalerite grains from Arre (Fig. 2). Therefore, the dissolution-reprecipitation model is unlikely to be responsible for the formation of briartite nanoscale inclusions.

The temperature conditions and amount of crystal-plastic deformation play an important role in determining the prevalent diffusion mechanism. During the Pyrenean-Alpine metamorphism, the sample experienced deformation and low-grade metamorphism (<400 °C; Cugerone et al., 2021). The APT specimens were prepared from several areas, including a weakly deformed domain with no low-angle boundaries in proximity (APT specimen 18 and 19; Fig. 2F). In the APT atom maps, the briartite inclusions are not spatially associated with dislocations in 3D, usually observable as linear features decorated with trace elements (Fig. 4; Fougerouse et al., 2019, 2021; Verberne et al., 2022). Instead, the inclusions are isolated within the sphalerite matrix. Therefore our data do not support a link between trace element mobility and deformation microstructures and, by extension, short-circuit diffusion pathways or defect-impurity pair diffusion models (Mehrer, 2007). The Pyrenean-Alpine metamorphism conditions (<400 °C) may have been high enough for the solid-state diffusion of Cu

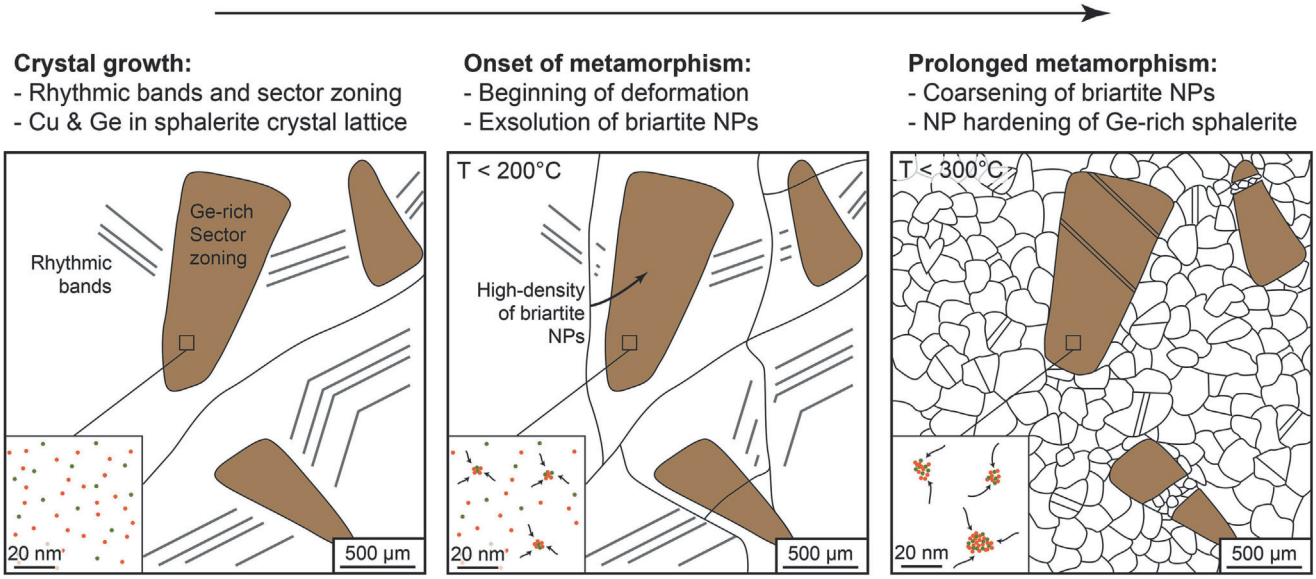

Fig. 6. Schematic diagram showing the evolution of Ge-bearing sphalerite during metamorphism and recrystallization. In the nanoscale insets, the green spheres represent Ge atoms and the orange spheres Cu atoms. (For interpretation of the references to colour in this figure legend, the reader is referred to the web version of this article.)

and Ge and the exsolution of briartite (Fig. 6), as suggested in the Kipushi deposit (De Vos et al., 1974). The GGIMFis geothermometer is generally used to estimate formation temperature of sphalerite based on the concentration of Ga, Ge, Fe, Mn and In (Frenzel et al., 2016). Application of this geothermometer on sphalerite is only possible if these concentrations are hosted in sphalerite crystallographic lattice (Frenzel et al., 2016). The Arre epigenetic Zn-Pb mineralisation was metamorphosed at greenschist facies conditions (<400 °C). However, the presence of nanoscale briartite inclusions precludes the use of GGIMFis geothermometer and may explain why the GGIMFis geothermometer does not record temperature greater than 310 °C as observed by Frenzel et al. (2016). The determination of diffusion coefficients for Cu and Ge in sphalerite or the study of metamorphosed deposits with at know conditions would be necessary to test if solid-state diffusion alone can be responsible for the nanoscale heterogeneities observed, or if another mechanism is necessary.

5.3. Implications

Combined petrographic, EBSD, LIBS and APT analyses revealed that trace elements such as Ge, Ga, Cu, Ag, Sb and Sn are enriched in dark in transmitted light domains, and can be either contained in sphalerite solid solution in sphalerite or as briartite nanoscale inclusions. Previous studies on the same samples using LA-ICPMS, determined that the dark sector zones are depleted in Fe compared to other sphalerite domain that appear light in transmitted light (Belissont et al., 2014; Cugerone et al., 2021). Although nanoscale inclusions of briartite may explain the darker appearance of the sector zone due to light absorption or diffraction, the absence of nanoscale inclusions in Saint-Salvy indicate that nanoscale inclusions may not be the only factor influencing the colour of sphalerite in transmitted light microscopy.

The exsolution of briartite from sphalerite during metamorphism may have implication for the recrystallization of sphalerite during deformation and the remobilization of critical metals. Briartite nanoscale inclusions may affect the migration of dislocations during crystal-plastic deformation. Inclusions can pin dislocations and promote the nucleation of low- and high-angle boundaries (Tweed et al., 1984). However, a high density of nanoscale inclusions (between 20 and 100 nm) can harden materials and inhibit recrystallization (Gleiter, 1991). Therefore, sphalerite with a high content of trace elements, including critical metals, subjected to metamorphism may exsolve numerous nanoparticles and become more resilient to crystal-plastic deformation (Fig. 6). Recrystallization was interpreted as an important step for the redistribution of critical metals in sphalerite along low- and high-angle boundaries (Cugerone et al., 2020). In addition to this process, our results suggest that low-grade metamorphic conditions may be beneficial to preserve critical elements resource.

6. Conclusions

Using a multiscale approach, this study reveals that critical elements such as Ge and Ga are preferentially hosted in sector zones of sphalerite, compared to rhythmic bands. The nanoscale analysis of the unmetamorphosed Saint-Salvy sphalerite indicates that Ge and Ga are bound in the crystal lattice. In the Arre sphalerite, which were metamorphosed under greenschist facies conditions, Ge and Cu exsolved from the crystal lattice and formed nanoscale briartite inclusions. No detectable Ge remained in the sphalerite surrounding the nanoscale inclusions. It is proposed that the exsolution of briartite is a result of metamorphism and may explain the capping of the GMMIFis geothermometer at 310 °C, tracking the temperature of exsolution of briartite nanoparticles. Futhermore, it is proposed that the presence of a high density of briartite nanoparticles in sphalerite may increase the rigidity of sphalerite, prevent recrystallization, and promote preservation of critical elements resource.

Declaration of Competing Interest

The authors declare that they have no known competing financial interests or personal relationships that could have appeared to influence the work reported in this paper.

Acknowledgments

This study was funded by the Australian Research Council DE190101307 and the French region Rhônes Alpes Auvergne (Optolyse, CPER2016). Rémi Belissont is thanked for sharing raw LA-ICPMS geochemistry data of Saint-Salvy sphalerite. The authors acknowledge Christophe Nevado and Doriane Delmas for the thin sections preparation and Fabrice Barou for the acquisition of the EBSD analyses. We thank associate George Calas for editorial handling and the three anonymous reviewers for their constructive feedback.

Research Data

Research Data associated with this article can be accessed at https://doi.org/10.17632/dzvrpscbcg.1.

Appendix A. Supplementary material

The supplementary files include a representative APT mass spectra (Fig. S1), nearest neighbour distance distribution for Ag and Cu of Saint-Salvy APT specimen M20 (Fig. S2), additional LIBS maps for the Saint-Salvy sample (Fig. S3), as well as the specific LIBS line wavelengths (Table S2). Supplementary material to this article can be found online at https://doi.org/10.1016/j.gca.2023.02.011.

References

Baele, J.-M., Bouzahzah, H., Papier, S., Decrée, S., Verheyden, S., Burlet, C., Pirard, E., Franceschi, G., Dejonghe, L., 2021. Trace-element imaging at macroscopic scale in a Belgian sphalerite-galena ore using Laser-Induced Breakdown Spectroscopy (LIBS). Geol. Belg. 24.

Belissont, R., Boiron, M.-C., Luais, B., Cathelineau, M., 2014. LA-ICP-MS analyses of minor and trace elements and bulk Ge isotopes in zoned Ge-rich sphalerites from the Noailhac–Saint-Salvy deposit (France): Insights into incorporation mechanisms and ore deposition processes. Geochim. Cosmochim. Acta 126, 518–540.

Belissont, R., Muñoz, M., Boiron, M.-C., Luais, B., Mathon, O., 2016. Distribution and oxidation state of Ge, Cu and Fe in sphalerite by μ-XRF and K-edge μ-XANES: insights into Ge incorporation, partitioning and isotopic fractionation. Geochim. Cosmochim. Acta 177, 298–314.

Belissont, R., 2016. Germanium and related elements in sulphide minerals: crystal chemistry, incorporation and isotope fractionation. PhD dissertation.

Bonnet, J., Cauzid, J., Testemale, D., Kieffer, I., Proux, O., Lecomte, A., Bailly, L., 2017. Characterization of germanium speciation in sphalerite (ZnS) from Central and Eastern Tennessee, USA, by X-ray absorption spectroscopy. Minerals 7, 79.

Cáceres, J.O., Pelascini, F., Motto-Ros, V., Moncayo, S., Trichard, F., Panczer, G., Marín-Roldán, A., Cruz, J., Coronado, I., Martín-Chivelet, J., 2017. Megapixel multi-elemental imaging by Laser-Induced Breakdown Spectroscopy, a technology with considerable potential for paleoclimate studies. Sci. rep. 7, 1–11.

Clerc, C., Lahfid, A., Monié, P., Lagabrielle, Y., Chopin, C., Poujol, M., Boulvais, P., Ringenbach, J.-C., Masini, E., de St Blanquat, M., 2015. High-temperature metamorphism during extreme thinning of the continental crust: a reappraisal of the North Pyrenean passive paleomargin. Solid Earth 6, 643–668.

Cook, N.J., Ciobanu, C.L., Pring, A., Skinner, W., Shimizu, M., Danyushevsky, L., Saini-Eidukat, B., Melcher, F., 2009. Trace and minor elements in sphalerite: A LA-ICPMS study. Geochim. Cosmochim. Acta 73, 4761–4791.

Cugerone, A., Cenki-Tok, B., Chauvet, A., Le Goff, E., Bailly, L., Alard, O., Allard, M., 2018. Relationships between the occurrence of accessory Ge-minerals and sphalerite in Variscan Pb-Zn deposits of the Bossost anticlinorium, French Pyrenean Axial Zone: Chemistry, microstructures and ore-deposit setting. Ore Geol. Rev. 95, 1–19.

Cugerone, A., Cenki-Tok, B., Oliot, E., Muñoz, M., Barou, F., Motto-Ros, V., Le Goff, E., 2020. Redistribution of germanium during dynamic recrystallization of sphalerite. Geology 48, 236–241.

Cugerone, A., Cenki-Tok, B., Munoz, M., Kouzmanov, K., Oliot, E., Motto-Ros, V., Le Goff, E., 2021. Behavior of critical metals in metamorphosed Pb-Zn ore deposits: example from the Pyrenean Axial Zone. Miner. Deposita 56, 685–705.

De Vos, W., Viaene, W., Moreau, J., Wautier, J., 1974. Mineralogie du gisement de Kipushi, Shaba, Zaire. Annales de la Société géologique de Belgique.

Dubosq, R., Rogowitz, A., Schneider, D., Schweinar, K., Gault, B., 2021. Fluid inclusion induced hardening: nanoscale evidence from naturally deformed pyrite. Contrib. Mineral. Petrol. 176, 1–14.

Fanlo, I., Touray, J., Subías, I., Fernández-Nieto, C., 1998. Geochemical patterns of a sheared fluorite vein, Parzan ,Spanish Central Pyrenees. Mineral. Deposita 33, 620–632.

Fougerouse, D., Reddy, S.M., Saxey, D.W., Rickard, W.D., Van Riessen, A., Micklethwaite, S., 2016a. Nanoscale gold clusters in arsenopyrite controlled by growth rate not concentration: Evidence from atom probe microscopy. Am. Mineral. 101, 1916–1919.

Fougerouse, D., Micklethwaite, S., Tomkins, A.G., Mei, Y., Kilburn, M., Guagliardo, P., Fisher, L.A., Halfpenny, A., Gee, M., Paterson, D., 2016b. Gold remobilisation and formation of high grade ore shoots driven by dissolution-reprecipitation replacement and Ni substitution into auriferous arsenopyrite. Geochim. Cosmochim. Acta 178, 143–159.

Fougerouse, D., Reddy, S.M., Kirkland, C.L., Saxey, D.W., Rickard, W.D., Hough, R.M., 2019. Time-resolved, defect-hosted, trace element mobility in deformed Witwatersrand pyrite. Geosci. Front. 10, 55–63.

Fougerouse, D., Reddy, S.M., Aylmore, M., Yang, L., Guagliardo, P., Saxey, D.W., Rickard, W.D., Timms, N., 2021. A new kind of invisible gold in pyrite hosted in deformation-related dislocations. Geology 49, 1225–1229.

Fougerouse, D., Saxey, D.W., Rickard, W.D.A., Reddy, S.M., Verberne, R., 2022. Standardizing spatial reconstruction parameters for the atom probe analysis of common minerals. Microsc. Microanal. 28, 1221–1230.

Frenzel, M., Hirsch, T., Gutzmer, J., 2016. Gallium, germanium, indium, and other trace and minor elements in sphalerite as a function of deposit type—A meta-analysis. Ore Geol. Rev. 76, 52–78.

Frenzel, M., Cook, N.J., Ciobanu, C.L., Slattery, A.D., Wade, B.P., Gilbert, S., Ehrig, K., Burisch, M., Verdugo-Ihl, M.R., Voudouris, P., 2020. Halogens in hydrothermal sphalerite record origin of ore-forming fluids. Geology 48, 766–770.

Gleiter, H., 1991. Nanocrystalline materials. Springer, pp. 1–37.

Gopon, P., Douglas, J.O., Auger, M.A., Hansen, L., Wade, J., Cline, J.S., Robb, L.J., Moody, M.P., 2019. A nanoscale investigation of carlin-type gold deposits: an atom-scale elemental and isotopic perspective. Econ. Geol. 114, 1123–1133.

Gregory, D.D., Large, R.R., Halpin, J.A., Baturina, E.L., Lyons, T.W., Wu, S., Danyushevsky, L., Sack, P.J., Chappaz, A., Maslennikov, V.V., 2015. Trace element content of sedimentary pyrite in black shales. Econ. Geol. 110, 1389–1410.

Johan, Z., 1988. Indium and germanium in the structure of sphalerite: an example of coupled substitution with copper. Mineral. Petrol. 39, 211–229.

Johnson, C.A., Cardellach, E., Tritlla, J., Hanan, B., 1996. Cierco Pb-Zn-Ag vein deposits; isotopic and fluid inclusion evidence for formation during the Mesozoic extension in the Pyrenees of Spain. Econ. Geol. 91, 497–506.

Luo, K., Cugerone, A., Zhou, M.-F., Zhou, J.-X., Sun, G.-T., Xu, J., He, K.-J., Lu, M.-D., 2022. Germanium enrichment in sphalerite with acicular and euhedral textures: an example from the Zhulingou carbonate-hosted Zn (-Ge) depositm South China. Miner. Deposita, 1–23.

Mehrer, H., 2007. Diffusion in Solids: Fundamentals, Methods, Materials, Diffusion-controlled Processes. Springer Science & Business Media.

Motto-Ros, V., Moncayo, S., Trichard, F., Pelascini, F., 2019. Investigation of signal extraction in the frame of laser induced breakdown spectroscopy imaging. Spectrochim. Acta Part B: At. Spectrosc. 155, 127–133.

Munoz, M., Boyce, A.J., Courjault-Rade, P., Fallick, A.E., Tollon, F., 1994. Multi-stage fluid incursion in the Palaeozoic basement-hosted Saint-Salvy ore deposit (NW Montagne Noire, southern France). Appl. Geochem. 9, 609–626.

Munoz, M., Baron, S., Boucher, A., Béziat, D., Salvi, S., 2016. Mesozoic vein-type Pb–Zn mineralization in the Pyrenees: Lead isotopic and fluid inclusion evidence from the Les Argentières and Lacore deposits. C. R. Geosci. 348, 322–332.

Perea, D.E., Arslan, I., Liu, J., Ristanović, Z., Kovarik, L., Arey, B.W., Lercher, J.A., Bare, S.R., Weckhuysen, B.M., 2015. Determining the location and nearest neighbours of aluminium in zeolites with atom probe tomography. Nat. Commun. 6, 7589.

Philippe, T., De Geuser, F., Duguay, S., Lefebvre, W., Cojocaru-Mirédin, O., Da Costa, G., Blavette, D., 2009. Clustering and nearest neighbour distances in atom-probe tomography. Ultramicroscopy 109, 1304–1309.

Putnis, A., 2002. Mineral replacement reactions: from macroscopic observations to microscopic mechanisms. Mineral. Mag. 66, 689–708.

Putnis, A., Fernandez-Diaz, L., Prieto, M., 1992. Experimentally produced oscillatory zoning in the (Ba, Sr) SO_4 solid solution. Nature 358, 743–745.

Reddy, S.M., Hough, R.M., 2013. Microstructural evolution and trace element mobility in Witwatersrand pyrite. Contrib. Mineral. Petrol. 166, 1269–1284.

Reddy, S.M., Saxey, D.W., Rickard, W.D.A., Fougerouse, D., Montalvo, S.D., Verberne, R., van Riessen, A., 2020. Atom probe tomography: development and application to the geosciences. Geostand. Geoanal. Res. 44, 5–50.

Reyx, J., 1973. Relations entre Tectonique, Métamorphisme de Contact et Concentrations Metalliques dans le Secteur des Anciennes Mines d'Arre et Anglas (Hautes-Pyrénées-Pyrénées atlantiques). PhD Disertation University Paris VI Paris, France.

Schirmer, T., Ließmann, W., Macauley, C., Felfer, P., 2020. Indium and Antimony Distribution in a Sphalerite from the "Burgstaetter Gangzug" of the Upper Harz Mountains Pb-Zn Mineralization. Minerals 10, 791.

Subías, I., Fanlo, I., Yuste, A., Fernández-Nieto, C., 1999. The Yenefrito Pb-Zn mine (Spanish Central Pyrenees): an example of superimposed metallogenetic events. Miner. Deposita 34, 220–223.

Taylor, S.D., Gregory, D.D., Perea, D.E., Kovarik, L., Cliff, J.B., Lyons, T.W., 2022. Pushing the limits: Resolving paleoseawater signatures in nanoscale fluid inclusions by atom probe tomography. Earth Planet. Sci. Lett. 599, 117859.

Tiu, G., Jansson, N., Wanhainen, C., Ghorbani, Y., Lilja, L., 2021. Ore mineralogy and trace element (re) distribution at the metamorphosed Lappberget Zn-Pb-Ag-(Cu-Au) deposit, Garpenberg, Sweden. Ore Geol. Rev. 135, 104223.

Tweed, C., Ralph, B., Hansen, N., 1984. The pinning by particles of low and high angle grain boundaries during grain growth. Acta metall. 32, 1407–1414.

Verberne, R., Reddy, S.M., Saxey, D.W., Fougerouse, D., Rickard, W.D., Quadir, Z., Evans, N.J., Clark, C., 2022. Dislocations in minerals: Fast-diffusion pathways or trace-element traps? Earth Planet. Sci. Lett. 584, 117517.

Wei, C., Ye, L., Hu, Y., Danyushevskiy, L., Li, Z., Huang, Z., 2019. Distribution and occurrence of Ge and related trace elements in sphalerite from the Lehong carbonate-hosted Zn-Pb deposit, northeastern Yunnan, China: Insights from SEM and LA-ICP-MS studies. Ore Geol. Rev. 115, 103175.

White, S.J.O., Piatak, N.M., McAleer, R.J., Hayes, S.M., Seal II, R.R., Schaider, L.A., Shine, J.P., 2022. Germanium re distribution during weathering of Zn mine wastes: Implications for environmental mobility and recovery of a critical mineral. Appl. Geochem., 105341

Wu, Y.-F., Fougerouse, D., Evans, K., Reddy, S.M., Saxey, D.W., Guagliardo, P., Li, J.-W., 2019a. Gold, arsenic, and copper zoning in pyrite: A record of fluid chemistry and growth kinetics. Geology 47, 641–644.

Wu, Y.-F., Evans, K., Li, J.-W., Fougerouse, D., Large, R.R., Guagliardo, P., 2019b. Metal remobilization and ore-fluid perturbation during episodic replacement of auriferous pyrite from an epizonal orogenic gold deposit. Geochim. Cosmochim. Acta 245, 98–117.

Xia, F., Brugger, J., Chen, G., Ngothai, Y., O'Neill, B., Putnis, A., Pring, A., 2009. Mechanism and kinetics of pseudomorphic mineral replacement reactions: a case study of the replacement of pentlandite by violarite. Geochim. Cosmochim. Acta 73, 1945–1969.

Zwart, H., 1963. Metamorphic history of the Central Pyrenees, Part II. Valle de Arán, sheet 4. Leidse Geologische Mededelingen 28, 321–376.